Friction **12**(1): 110–119 (2024)
https://doi.org/10.1007/s40544-023-0738-6
ISSN 2223-7690
CN 10-1237/TH
RESEARCH ARTICLE

Comparative analysis of frictional behavior and mechanism of molybdenum ditelluride with different structures

Lina ZHANG, Xinfeng TAN*, Jianguo JIAO, Dan GUO, Jianbin LUO*
State Key Laboratory of Tribology in Advanced Equipment, Tsinghua University, Beijing 100084, China
Received: 21 October 2022 / Revised: 03 December 2022 / Accepted: 05 January 2023

Abstract: Two-dimensional (2D) transition metal dichalcogenides (TMDCs) have layered structures with excellent tribological properties. Since the energy difference between hexagonal-molybdenum ditelluride (2H-$MoTe_2$) and distorted octahedral-molybdenum ditelluride (1T′-$MoTe_2$) is very small among the transition metal dichalcogenides (TMDCs), $MoTe_2$ becomes one of the most promising candidates for phase engineering. In our experiment, we found that the friction force and friction coefficient (COF) of 2H-$MoTe_2$ were an order of magnitude smaller than those of 1T′-$MoTe_2$ by the atomic force microscope (AFM) experiments. The friction difference between 1T′-$MoTe_2$ and 2H-$MoTe_2$ was further verified in molecular dynamics (MD) simulations. The density functional theory (DFT) calculations suggest that the friction contrast is related to the difference in sliding energy barrier of the potential energy surface (PES) for a tip sliding across the surface. The PES obtained from the DFT calculation indicates that the maximum energy barrier and the minimum energy path (MEP) energy barrier of 2H-$MoTe_2$ are both smaller than those of 1T′-$MoTe_2$, which means that less energy needs to be dissipated during the sliding process. The difference in energy barrier of the PES could be ascribed to its larger interlayer spacing and weaker Mo–Te interatomic interactions within the layers of 2H-$MoTe_2$ than those of 1T′-$MoTe_2$. The obvious friction difference between 1T′-$MoTe_2$ and 2H-$MoTe_2$ not only provides a new non-destructive means to detect the phase transition by the AFM, but also provides a possibility to tune friction by controlling the phase transition, which has the potential to be applied in extreme environments such as space lubrication.

Keywords: friction; two-dimensional (2D) materials; distorted octahedral-molybdenum ditelluride (1T′-$MoTe_2$); hexagonal-molybdenum ditelluride (2H-$MoTe_2$); phase transition

1 Introduction

Two-dimensional (2D) materials have layered structures with weak van der waals forces between the adjacent atomic layers, which makes it easy to slide [1]. Among various 2D materials, transition metal dichalcogenides (TMDCs) have attracted considerable attention for their excellent tribological performance under extreme conditions such as space environment [2]. Although the frictional properties of MoS_2 have been extensively studied [3, 4], the frictional properties of other members of the TMDC family remain relatively unexplored. It has been shown that the friction force of molybdenum ditelluride ($MoTe_2$) is lower than those of MoS_2 and $MoSe_2$ under identical conditions [5]. Therefore, $MoTe_2$ has the potential to become one of the most promising materials for excellent frictional properties.

As the chalcogen elements (S, Se, and Te) in TMDCs have relatively small electronegativity, either covalent or ionic bonds may be formed, leading to the generation of structural polymorphs with different bonding configurations and close energy [6]. According to the density functional theory (DFT) calculations, semiconductor hexagonal (2H) and metallic distorted

* Corresponding authors: Xinfeng TAN, E-mail: txf_1993@126.com; Jianbin LUO, E-mail: luojb@mail.tsinghua.edu.cn

octahedral (1T′) phases of $MoTe_2$ can be stable at room temperature, and the energy difference between these two phases is about 38 meV for per formula $MoTe_2$ [7], which is very small among the TMDC family. It has been shown that weak non-chemical external stimuli, such as temperature [8], tensile strain [7, 9], laser irradiation [10, 11], plasma treatment [12], electrostatic doping [13], and electric fields [14], can drive the semiconductor-to-metal transition of the $MoTe_2$. It has been confirmed that inducing the transition from 2H-molybdenum ditelluride (2H-$MoTe_2$) to 1T′-molybdenum ditelluride (1T′-$MoTe_2$) can improve the contact quality of transistors [15] and promote the catalytic activity of hydrogen evolution reaction [16]. Consequently, $MoTe_2$ is considered as one of the most promising candidates for phase engineering.

The layered structure and diverse structural polymorphs of $MoTe_2$ imply abundant and even excellent frictional properties to some extent. However, the frictional behavior of $MoTe_2$ with different structures is not clear, especially for 1T′-$MoTe_2$. In fact, it has been the goal of scholars to effectively reduce friction, explain frictional behavior and mechanism, and achieve active regulation of friction. Among the mainstream friction regulation methods, strain-regulated friction [17] is limited by the magnitude of the load, and electric field-regulated friction [18] also has the limitation in the conductivity of materials, so new regulation methods need to be studied. Potentially, since the properties of different phases vary greatly, the use of phase transitions is an ideal method to achieve the modulation of friction properties. Therefore, the study of the frictional properties of $MoTe_2$ with different structures is particularly urgent.

Here, the frictional behavior of 1T′-$MoTe_2$ and 2H-$MoTe_2$ was investigated experimentally and theoretically, and the reasons for the lower friction force and friction coefficient (COF) of 2H-$MoTe_2$ than those of 1T′-$MoTe_2$ were explained in depth from the perspective of energy. The frictional contrast existing between these two phases illustrates that the 1T′-$MoTe_2$ and 2H-$MoTe_2$ can be distinguished nondestructively by measuring the atomic friction. The study of the frictional behavior of $MoTe_2$ with different structures shows that the frictional behavior of different phases varies greatly due to the different atomic arrangements, indicating that the friction can be modified by changing the atomic arrangements, such as controlling the semiconductor–metal transition of $MoTe_2$.

2 Experiments and simulations

2.1 Sample preparation and characterization

The substrate was a die cut from a Si(100) wafer with about 300 nm of thermally grown SiO_2. Both 1T′-$MoTe_2$ and 2H-$MoTe_2$ crystals (HQ Graphene, the Netherlands) were transferred to a silicon wafer by mechanical exfoliation assisted by polydimethylsiloxane [19]. The optical images (acquired by Olympus BX60 microscope with Canon DS126431 camera) of the samples are shown in Figs. 1(a) and 1(b). The thickness of the sample was measured using a commercial atomic force microscope (AFM; Cypher S, Asylum Research, Oxford Instruments) in contact mode. The thicknesses of friction regions of the 1T′-$MoTe_2$ and 2H-$MoTe_2$ were 39 and 32 nm, respectively. To further confirm the compositions of these two materials, the Raman spectra (LabRAM HR evolution, HORIBA; 514 nm) were applied to characterize the $MoTe_2$ flakes. As shown in Fig. 1(c), characteristic peaks of 1T′-$MoTe_2$ (A_g at 111 cm^{-1}, B_g at 164 cm^{-1}, and A_g at 259 cm^{-1}) can be clearly seen. Besides, the Raman characteristic peaks (A_1' at 173 cm^{-1} and E′ at 234 cm^{-1}) are attributed to the 2H-$MoTe_2$ [20], as shown in Fig. 1(d). The characteristic peaks are in good agreement with their theoretical values, which proves the purity of the material.

2.2 Friction force measurements

Friction measurements were carried out using the AFM under ambient conditions. The normal and lateral force constants of the silicon probe (PPP-LFMR, Nanosensors) were calibrated using the thermal noise method and improved wedge calibration method [21], respectively. The spring constant of the probe is about 0.26 N/m, and the lateral force constant is nearly 341 nN/V. In the lateral force mode, friction maps were measured with gradient loading applied to a square region of 200 nm × 200 nm with a scanning frequency of 2 Hz, as shown in Figs. 2(a) and 2(b). The friction force

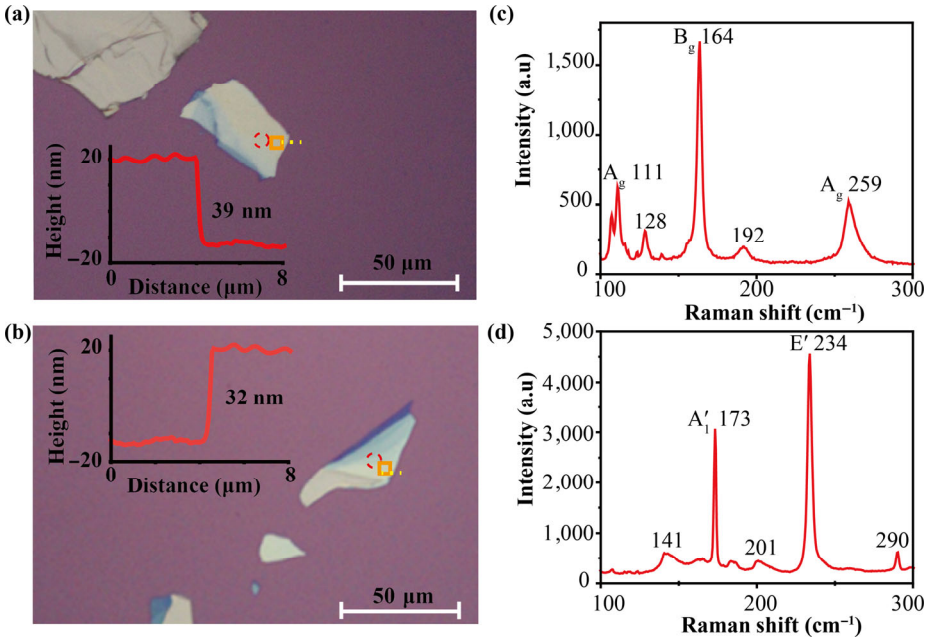

Fig. 1 Characterizations of $MoTe_2$. Optical microscope images of (a) 1T′-$MoTe_2$ and (b) 2H-$MoTe_2$ on SiO_2/Si substrates. The insets of (a) and (b) show the height profiles along the yellow dashed lines measured by the AFM. Raman spectra of (c) 1T′-$MoTe_2$ and (d) 2H-$MoTe_2$ obtained from the areas shown in the red dashed circles in (a) and (b), respectively. Friction experiments were carried out in the area shown in the orange boxes of (a) and (b).

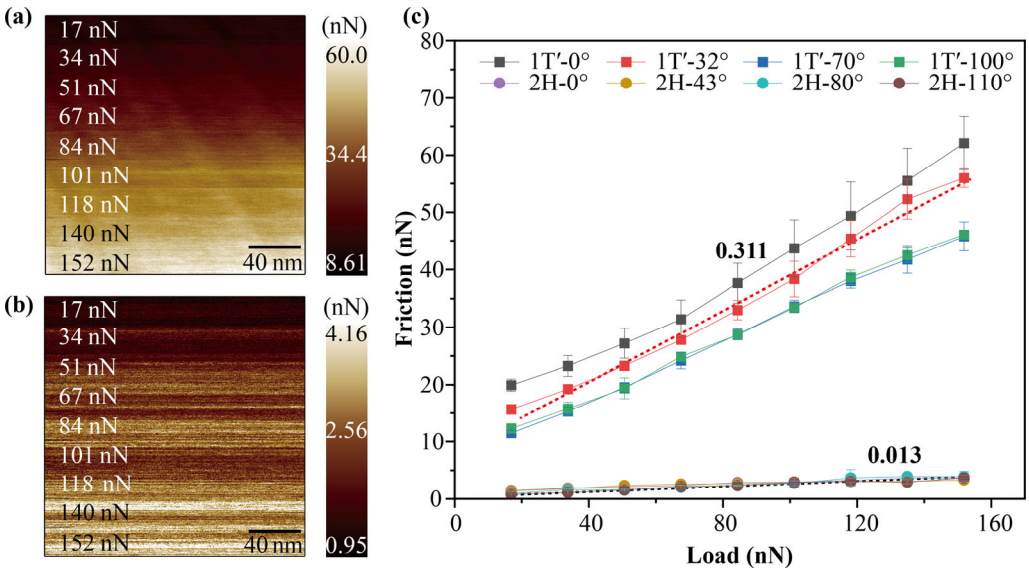

Fig. 2 Friction force measurements using the AFM. Mappings of friction forces at different loads for (a) 1T′-$MoTe_2$ and (b) 2H-$MoTe_2$. (c) Variations of friction force with load at different rotation angles of samples. The error bars show the standard errors over three sliding cycles. The dashed lines show the linear fits to the data, and the marked slopes are the COFs.

of 1T′-$MoTe_2$ showed significant variation with the change of load. When the load changed from 17 to 152 nN, the friction force changed from 8.61 to 60.0 nN. In contrast, the friction map of 2H-$MoTe_2$ varies slightly with gradient loading. In order to understand the relationship between the friction force and the friction direction, the relative angles of the sample and the probe were changed by rotating the sample. In addition, three different locations were selected for friction measurements under each condition, and the variations of friction force with load were obtained, as shown in Fig. 2(c). For 2H-$MoTe_2$, the difference of

friction force with angles at 0°, 43°, 80°, and 110° of sample rotation was small, and the friction force can be considered isotropic. When the angles of the 1T′-$MoTe_2$ sample were varied to 0°, 32°, 70°, and 100°, the difference in adhesion had some degree of influence on the magnitude of the friction force, but the overall trend of friction was not very different. Since the friction difference between 1T′-$MoTe_2$ and 2H-$MoTe_2$ was concerned, the anisotropy of frictional force was no longer considered. It can be found that the frictional force of the 2H phase was one order of magnitude smaller than that of the 1T′ phase. The COF of 1T′-$MoTe_2$ was 0.311, while that of 2H-$MoTe_2$ was only 0.013, which can be obtained by performing a linear fit to the data.

By further reducing the scan range to 20 nm × 20 nm and increasing the scanning frequency to 20 Hz, the friction maps including atomic-scale stick–slip motion information were obtained, as shown in Figs. 3(a) and 3(f). The reciprocal lattice information (Figs. 3(b) and 3(g)) is obtained by the two-dimensional fast Fourier transform (2D FFT) analysis of Figs. 3(a) and 3(f). However, the lattice in the magnitude/modulus maps obtained by the 2D FFT is a reciprocal lattice, which should be transferred to real space. Lattice vectors as well as the angles between the two vectors of the real lattice were obtained after the transformation following the formula [22].

The measured lattice basis vectors and angles in the real lattice of 1T′-$MoTe_2$ were 6.0 Å, 3.5 Å and 83°, which were similar to the theoretical values of 6.4 Å, 3.5 Å, and 90°. Similarly, as for 2H-$MoTe_2$, the measured

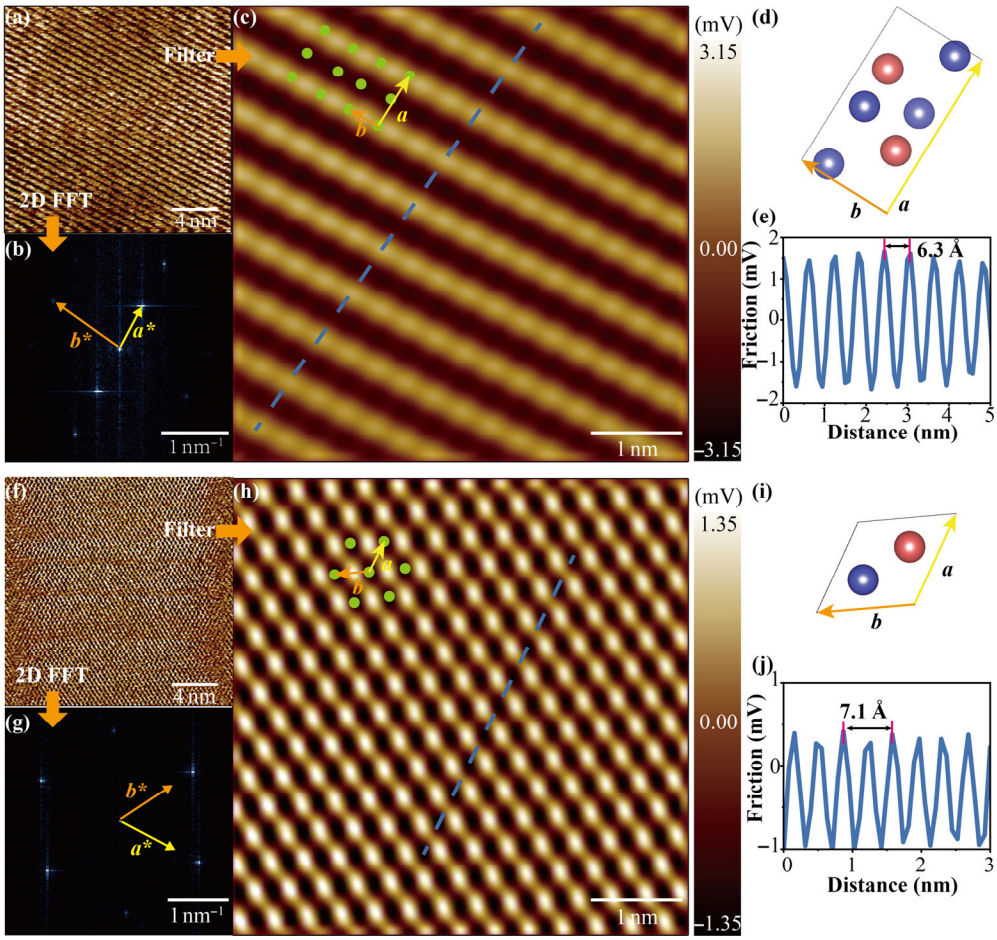

Fig. 3 Atomic-scale friction maps of $MoTe_2$. (a) Mapping of friction signal of 1T′-$MoTe_2$. (b) Reciprocal lattice obtained by 2D FFT on (a). (c) Atomic-level stick–slip map obtained by FFT filtering of (a). (d) Unit cell structure of 1T′-$MoTe_2$. (e) Friction profile extracted along the blue dashed line in (c). (f) Mapping of friction signal of 2H-$MoTe_2$. (g) Reciprocal lattice obtained by 2D FFT on (f). (h) Atomic-level stick–slip map obtained by FFT filtering of (f). (i) Unit cell structure of 2H-$MoTe_2$. (j) Friction profile extracted along the blue dashed line in (h).

values of 3.6 Å, 3.6 Å, and 118° matched well with the theoretical values of 3.5 Å, 3.5 Å, and 120°. The difference between measured and theoretical values was most likely due to lattice distortion caused by the presence of the load. Moreover, high-resolution atomic-scale stick–slip maps can be achieved after filtering from friction maps, as shown in Figs. 3(c) and 3(h). The atomic-scale stick–slip map of 1T′-$MoTe_2$ showed the characteristics of a square structure, which was very similar to the unit-cell structure (Fig. 3(d)). A six-membered ring structure is observed in Fig. 3(h), which was consistent with the unit-cell parameters of 2H-$MoTe_2$, as shown in Fig. 3(i). The friction profiles (Figs. 3(e) and 3(j)) are extracted from Figs. 3(c) and 3(h), respectively, corresponding to the blue dashed lines. The period of atomic stick–slip was 6.3 Å for 1T′-$MoTe_2$ and 3.55 Å for 2H-$MoTe_2$, which were in good agreement with their lengths of the lattice basis vectors. Obviously, 1T′-$MoTe_2$ exhibited larger atomic scale friction than 2H-$MoTe_2$ in atomic-scale stick–slip. In general, the 2D FFT and filtering of atomic-scale stick–slip friction maps can reveal the friction process and distinguish the two materials with no damage.

2.3 Molecular dynamics (MD) simulation

In order to ensure the reliability of the experimental results, MD simulations were carried out. The MD model consisted of four layers of $MoTe_2$, which was obtained from the optimized structure. The atoms of bottom layer were fixed as the boundary, while the rest atoms were set as the thermostatic atomic layer with a Langevin thermostat maintained at a temperature of 300 K. The periodic boundary condition was used in x and y directions, and the fixed boundary condition was adopted in the z direction. To compare the frictional behavior of these two materials, the reactive force filed (ReaxFF) potential function [23] was chosen to describe the interaction between Mo and Te atoms for both materials. In order to be compatible with the ReaxFF potential function, the fix indent command was used to realize the simulation of the friction process. The indenter with a radius of 2 nm acted as virtual spherical probes and slid at a constant speed of 10 m/s in the x direction in 0.25 ns, as shown in the inset of Fig. 4(c). The magnitude of the applied load was adjusted by the press-in depth of indenter, and the forces on the indenter in x and z directions were recorded as friction and load, respectively. All MD simulations were performed using the Large-Scale Atomic/Molecular Massively Parallel Simulator (LAMMPS) [24], and the visualization was displayed and analyzed using the OVITO (version 3.3.5, OVITO GmbH) and VESTA (version3, JP-Minerals) softwares [26].

As shown in Figs. 4(a) and 4(b), the indenter slid over the material surfaces along the direction shown by the arrow. The variations of friction force with load during sliding are shown in Fig. 4(c). Obviously,

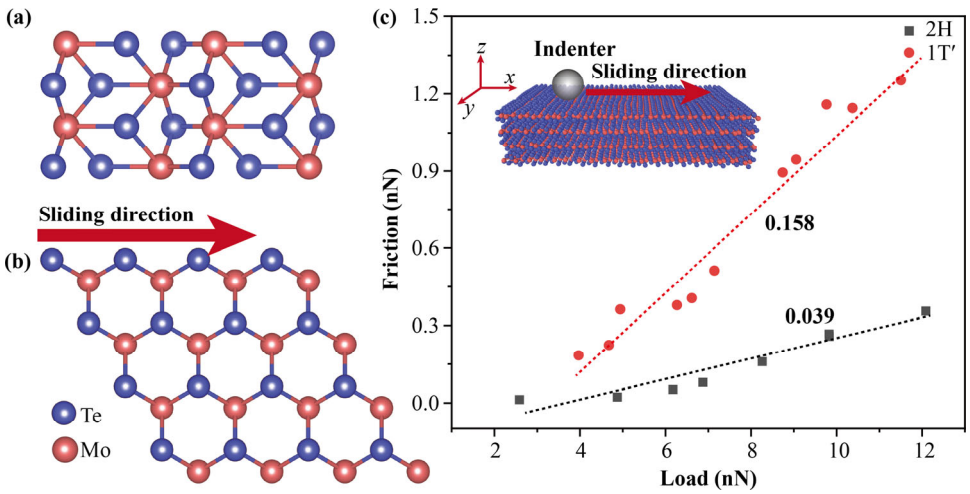

Fig. 4 MD simulations of friction process. Top view of atom arrangement of uppermost layers of $MoTe_2$: (a) 1T′-$MoTe_2$ and (b) 2H-$MoTe_2$ MD models. (c) Variations of friction force with load obtained from MD simulation. The inset in the upper left corner is the schematic diagram of the simulation. The dashed lines show the linear fits to the data, and the marked slopes are the COFs.

the friction force of the 2H phase was always smaller than that of the 1T′ phase, and the COFs obtained from the fitting curves were 0.039 and 0.158, respectively. Although the simulation conditions could not match the experiments precisely due to computational limitations, the results obtained from the simulation were congruent with the experimental results in trend. In summary, the results of the MD simulations further confirmed the reliability of the experimental results.

3 Discussion

During the friction measurement, materials were measured under the same environment and condition, so the temperature, humidity, and velocity of the experiment were not the main reasons of the friction difference between 1T′-$MoTe_2$ and 2H-$MoTe_2$. In addition, the friction force did not change significantly with tip wear in the experiment, and the MD simulation did not include the influence of the tip wear, so both the wear and elastic deformation of the tip were not the dominant mechanism as well. Furthermore, since the friction force was closely related to the surface roughness of the material, the difference of the surface roughness in the friction areas of these two materials was measured to be within 0.25 nm (root-mean-square roughness), which was not sufficient to produce such a significant friction contrast.

To further analyze the reason for the friction contrast between 1T′-$MoTe_2$ and 2H-$MoTe_2$, the DFT calculations were carried out using the Vienna *ab initio* Simulation Package (VASP; version 5.4.4, Hafner) [27]. For all the DFT calculations, the exchange correlation terms were treated by the Perdew–Berke–Ernzerhof (PBE) [28] form of the generalized gradient approximation (GGA). Standard VASP projector augmented-wave (PAW) [29] potentials were used to describe Mo, Te, C, and H. Among van der Waals corrections, the optB88-vdW function [30] was further used for calculating the sliding energy. A single methane (CH_4) molecule was used, acting as the probe in the AFM experiment, to simulate the friction process [31]. A model containing a supercell of 288 atoms and a CH_4 molecule was constructed to avoid interactions between neighboring CH_4 molecules. Moreover, a vacuum region of 15 Å was set up in the z direction to avoid the interaction between adjacent supercells in the z direction. After convergence test calculations, the plane-wave basis kinetic energy cutoff was set to be 500 eV, and the Brillouin zone was sampled by a Monkhorst–Pack [32] k-point mesh of 1 × 1 × 1. The electronic self-consistent calculations were converged within 10^{-5} eV. The internal structure relaxations stopped when the residual force on each atom was less than 0.01 eV/Å. The bilayer $MoTe_2$ and CH_4 molecules were first optimized separately, and then combined for structural optimization. For calculating the sliding energy, the atoms of the $MoTe_2$ were fixed for VASP selective dynamics, while the CH_4 molecule was displaced at different positions, restricting the degree of freedom of the in-plane positions [33–35].

The potential energy surfaces (PESs) (Figs. 5(a) and 5(b)) display different patterns corresponding to their lattice structures. The maximum energy barrier of 1T′-$MoTe_2$ is 53.80 meV, which is more than twice as large as that of 2H-$MoTe_2$ (22.20 meV). Therefore, in a random sliding process, the maxmium potential barrier that 2H-$MoTe_2$ needed to overcome was smaller than that of 1T′-$MoTe_2$, implying less energy dissipation and smaller friction force [36]. For the case of a specific friction path, the process of sliding along the minimum energy path (MEP) was analyzed. The MEP of 1T′-$MoTe_2$ was corresponding to the arrow (Fig. 5(a)), starting from A1, passing through A2, and ending at A3. Corresponding to the atomic structure, as shown in the inset of Fig. 5(c), CH_4 molecule moved from the initial molecular structure position, and then moved along the arrow to end at the CH_4 structure. For 2H-$MoTe_2$, the MEP moved from B1 (Fig. 5(b)) in the direction of the arrow, passed B2, and ended at point B3. The corresponding path in the atomic structure is shown in the inset of Fig. 5(d). The potential energy profiles along the MEP are shown in Figs. 5(c) and 5(d). The minimum energy barrier of 1T′-$MoTe_2$ (9.3 meV) was nearly twice as large as that of 2H-$MoTe_2$ (5.7 meV), which showed good consistency with the maximum energy barrier. The differences that exist on the maximum energy barrier and MEP energy barrier were an intuitive explanation for the friction difference between these two phases of $MoTe_2$.

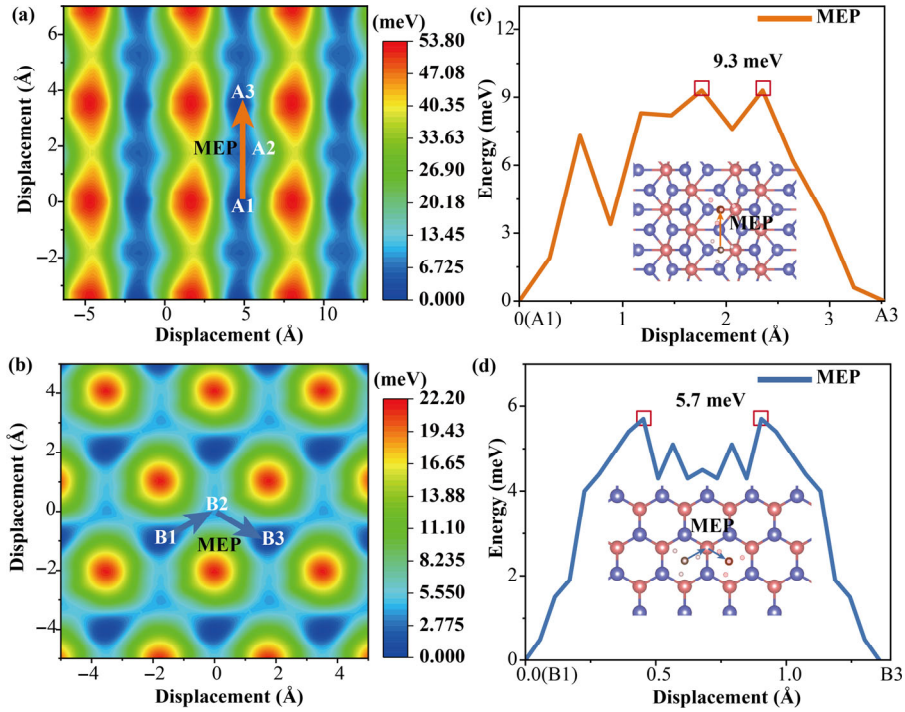

Fig. 5 DFT simulations of PES distribution of $MoTe_2$. PESs of bilayer (a) 1T′-$MoTe_2$ and (b) 2H-$MoTe_2$ with CH_4 molecule at the top. The arrows and letters marked in (a) and (b) indicate the routes of MEPs. Relative energy barriers calculated for translation of CH_4 along the path indicated by the arrows for (c) 1T′-$MoTe_2$ and (d) 2H-$MoTe_2$. The insets (in (c) and (d)) represent the sliding paths of CH_4 along the MEP, where the positions at the beginning of the arrows are the initial positions of the CH_4 molecule and the structures at the termination of the arrows are the final positions of the CH_4 molecule.

To investigate the effect of charge distribution on the PES, the charge distributions of the bilayer $MoTe_2$ with optimized geometries were calculated, as shown in Figs. 6(a) and 6(b). In the three-dimensional (3D) charge distribution plots, more charges distributed around atoms, especially Mo atoms. The 2D charge analysis was performed on the (010) crystal plane of the 1T′ phase and the (100) crystal plane of the 2H phase. The charge density around Mo atoms was higher than that of Te atoms, and the isoelectric surface around the Mo atoms of 2H-$MoTe_2$ was closer to a sphere in appearance. The comparison of the two systems indicated that the charge density in the 2D plane showed relatively small differences. Moreover, the influence of electrons was not considered in the MD simulation, so the difference in charge densities was not the main reason for the difference of friction characteristics of the two phases. By analyzing the optimized crystal structures of both phases after the DFT simulations, as shown in Figs. 6(c) and 6(d), it was found that the atomic arrangement of the 1T′ phase was relatively disordered compared to that of the 2H phase, which indicated that both the bond lengths and the bond angles were different. The DFT simulations showed that the cohesion energy [37] of the 2H-$MoTe_2$ was 20.06 meV, smaller than that of the 1T′-$MoTe_2$ per $MoTe_2$ formula unit, which means that the energy required to break the chemical bond between Mo and Te atoms was lower, and the intra-layer interaction was weaker. Besides, the interlayer distance (d = 7.002 Å, the minimum distance between Mo atoms of adjacent layers [33]) of 2H-$MoTe_2$ was larger than that of the 1T′ phase (d = 6.679 Å). The larger d indicates weaker interlayer interactions, which contributes to the decrease of friction [33, 38]. The DFT simulations showed that the interlayer binding energy of the 2H phase was 4.77 meV, smaller than that of the 1T′ phase per $MoTe_2$ formula unit. In summary, the weaker interactions between Mo and Te atoms and the larger layer spacing of 2H-$MoTe_2$ lead to a smaller PES barrier for 1T′-$MoTe_2$, causing a smaller friction force than that of the 1T′-$MoTe_2$.

Some differences can be found between experiments and simulations. When simulations were performed

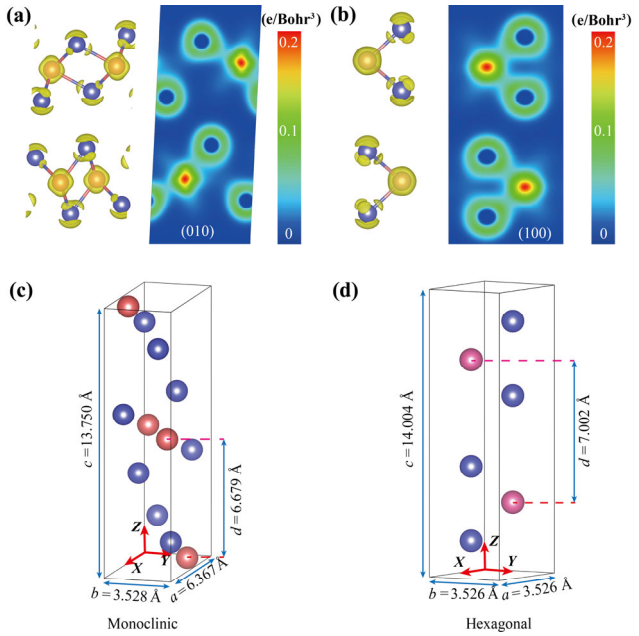

Fig. 6 Charge density distributions and atomic structures of $MoTe_2$. Charge density distributions of (a) 1T′-$MoTe_2$ and (b) 2H-$MoTe_2$; the isocharged surface is 0.08 e/Bohr^3 for 3D. 2D charge density distributions are the (010) plane for 1T′-$MoTe_2$ and the (100) plane for 2H-$MoTe_2$. Optimized unit cell structures for (c) 1T′-$MoTe_2$ and (d) 2H-$MoTe_2$. The d is defined as the distance between the two closest Mo atoms of the two adjacent layers.

based on experimental conditions, there were some reasonable simplifications between the model and the actual conditions due to the limitations of computational power and computational cost, such as neglecting the influence of tip materials when performing MD simulations and replacing the AFM probe by a CH_4 molecule when performing the DFT simulations. These reasonable simplifications were unavoidable, which leads to differences between experiments and simulations. In general, although the specific numerical relationships do not match perfectly, the simulation and experimental results are in good agreement in terms of trends and can explain the experimental friction behavior intuitively based on simplifying certain conditions.

4 Conclusions

In summary, it was found that the friction of 2H-$MoTe_2$ was an order of magnitude smaller than that of 1T′-$MoTe_2$, and the COFs were 0.013 and 0.311, respectively. The DFT calculations revealed that the difference between the PES barriers of these two materials was found to be the intuitive explanation for the friction difference. The larger d and weaker interactions between Mo and Te atoms of the 2H-$MoTe_2$ were the deeper reasons for the smaller friction force than that of the 1T′-$MoTe_2$. The differences in friction between different structural phases of $MoTe_2$ indicate a close relationship between friction and atomic arrangement, which suggests that friction can be actively regulated by controlling the phase transition.

Acknowledgements

This work was supported by the National Natural Science Foundation of China (Grant No. 52175175) and the Strategic Priority Research Program of the Chinese Academy of Sciences (Grant No. XDC04000000).

Declaration of competing interest

The authors have no competing interests to declare that are relevant to the content of this article. The author Jianbin LUO is the Editor-in-Chief of this journal.

References

[1] Liu L C, Zhou M, Jin L, Li L C, Mo Y T, Su G S, Li X, Zhu H W, Tian Y. Recent advances in friction and lubrication

of graphene and other 2D materials: Mechanisms and applications. *Friction* **7**(3): 199–216 (2019)

[2] Luo J B, Zhou X. Superlubricitive engineering—Future industry nearly getting rid of wear and frictional energy consumption. *Friction* **8**(4): 643–665 (2020)

[3] Meng Y G, Xu J, Ma L R, Jin Z M, Prakash B, Ma T B, Wang W Z. A review of advances in tribology in 2020–2021. *Friction* **10**(10): 1443–1595 (2022)

[4] Wu S C, Meng Z S, Tao X M, Wang Z. Superlubricity of molybdenum disulfide subjected to large compressive strains. *Friction* **10**(2): 209–216 (2022)

[5] Vazirisereshk M R, Hasz K, Zhao M Q, Johnson A T C, Carpick R W, Martini A. Nanoscale friction behavior of transition-metal dichalcogenides: Role of the chalcogenide. *ACS Nano* **14**(11): 16013–16021 (2020)

[6] Li W B, Qian X F, Li J. Phase transitions in 2D materials. *Nat Rev Mater* **6**(9): 829–846 (2021)

[7] Duerloo K A N, Li Y, Reed E J. Structural phase transitions in two-dimensional Mo- and W-dichalcogenide monolayers. *Nat Commun* **5**: 4214 (2014)

[8] Empante T A, Zhou Y, Klee V, Nguyen A E, Lu I H, Valentin M D, Naghibi Alvillar S A, Preciado E, Berges A J, Merida C S, et al. Chemical vapor deposition growth of few-layer $MoTe_2$ in the 2H, 1T′, and 1T phases: Tunable properties of $MoTe_2$ films. *ACS Nano* **11**(1): 900–905 (2017)

[9] Song S, Keum D H, Cho S, Perello D, Kim Y, Lee Y H. Room temperature semiconductor–metal transition of $MoTe_2$ thin films engineered by strain. *Nano Lett* **16**(1): 188–193 (2016)

[10] Tan Y, Luo F, Zhu M J, Xu X L, Ye Y, Li B, Wang G, Luo W, Zheng X M, Wu N N, et al. Controllable 2H-to-1T′ phase transition in few-layer $MoTe_2$. *Nanoscale* **10**(42): 19964–19971 (2018)

[11] Kang S, Won D, Yang H, Lin C H, Ku C S, Chiang C Y, Kim S, Cho S. Phase-controllable laser thinning in $MoTe_2$. *Appl Surf Sci* **563**: 150282 (2021)

[12] Nan H Y, Jiang J E, Xiao S Q, Chen Z R, Luo Z Z, Zhang L F, Zhang X M, Qi H, Gu X F, Wang X R, et al. Soft hydrogen plasma induced phase transition in monolayer and few-layer $MoTe_2$. *Nanotechnology* **30**(3): 034004 (2019)

[13] Wang Y, Xiao J, Zhu H Y, Li Y, Alsaid Y, Fong K Y, Zhou Y, Wang S Q, Shi W, Wang Y, et al. Structural phase transition in monolayer $MoTe_2$ driven by electrostatic doping. *Nature* **550**(7677): 487–491 (2017)

[14] Zhang F, Zhang H R, Krylyuk S, Milligan C A, Zhu Y Q, Zemlyanov D Y, Bendersky L A, Burton B P, Davydov A V, Appenzeller J. Electric-field induced structural transition in vertical $MoTe_2$- and $Mo_{1-x}W_xTe_2$-based resistive memories. *Nat Mater* **18**(1): 55–61 (2019)

[15] Cho S, Kim S, Kim J H, Zhao J, Seok J, Keum D H, Baik J, Choe D H, Chang K J, Suenaga K, et al. Phase patterning for ohmic homojunction contact in $MoTe_2$. *Science* **349**(6248): 625–628 (2015).

[16] McGlynn J C, Dankwort T, Kienle L, Bandeira N A G, Fraser J P, Gibson E K, Cascallana-Matías I, Kamarás K, Symes M D, Miras H N, et al. The rapid electrochemical activation of $MoTe_2$ for the hydrogen evolution reaction. *Nat Commun* **10**(1): 4916 (2019)

[17] Zhang S A, Hou Y A, Li S Z, Liu L Q, Zhang Z, Feng X Q, Li Q Y. Tuning friction to a superlubric state via in-plane straining. *PNAS* **116**(49): 24452–24456 (2019)

[18] He F, Yang X A, Bian Z L, Xie G X, Guo D, Luo J B. In-plane potential gradient induces low frictional energy dissipation during the stick–slip sliding on the surfaces of 2D materials. *Small* **15**(49): 1904613 (2019)

[19] Castellanos-Gomez A, Buscema M, Molenaar R, Singh V, Janssen L, van der Zant H S J, Steele G A. Deterministic transfer of two-dimensional materials by all-dry viscoelastic stamping. *2D Mater* **1**(1): 011002 (2014)

[20] Kan M, Nam H G, Lee Y H, Sun Q. Phase stability and Raman vibration of the molybdenum ditelluride ($MoTe_2$) monolayer. *Phys Chem Chem Phys* **17**(22): 14866–14871 (2015)

[21] Varenberg M, Etsion I, Halperin G. An improved wedge calibration method for lateral force in atomic force microscopy. *Rev Sci Instrum* **74**(7): 3362–3367 (2003)

[22] Hammond C. *The Basics of Crystallography and Diffraction*, 4th edn. Oxford (UK): Oxford University Press, 2015.

[23] Onofrio N, Guzman D, Strachan A. The dynamics of copper intercalated molybdenum ditelluride. *J Chem Phys* **145**(19): 194702 (2016)

[24] Plimpton S. Fast parallel algorithms for short-range molecular dynamics. *J Comput Phys* **117**(1): 1–19 (1995)

[25] Stukowski A. Visualization and analysis of atomistic simulation data with OVITO—The Open Visualization Tool. *Modelling Simul Mater Sci Eng* **18**(1): 015012 (2010)

[26] Momma K, Izumi F. VESTA: A three-dimensional visualization system for electronic and structural analysis. *J Appl Crystallogr* **41**(3): 653–658 (2008)

[27] Kresse G, Furthmüller J. Efficiency of *ab-initio* total energy calculations for metals and semiconductors using a plane-wave basis set. *Comput Mater Sci* **6**(1): 15–50 (1996)

[28] Perdew J P, Burke K, Ernzerhof M. Generalized gradient approximation made simple. *Phys Rev Lett* **77**(18): 3865–3868 (1996)

[29] Blöchl P E. Projector augmented-wave method. *Phys Rev B* **50**(24): 17953–17979 (1994)

[30] Klimeš J, Bowler D R, Michaelides A. Chemical accuracy for the van der Waals density functional. *J Phys Condens Matter* **22**(2): 022201 (2010)

[31] Vazirisereshk M R, Ye H, Ye Z J, Otero-de-la-Roza A, Zhao M Q, Gao Z L, Johnson A T C, Johnson E R, Carpick R W, Martini A. Origin of nanoscale friction contrast between supported graphene, MoS_2, and a graphene/MoS_2 heterostructure. *Nano Lett* **19**(8): 5496–5505 (2019)

[32] Monkhorst H J, Pack J D. Special points for Brillouin-zone integrations. *Phys Rev B* **13**(12): 5188–5192 (1976)

[33] Levita G, Molinari E, Polcar T, Righi M C. First-principles comparative study on the interlayer adhesion and shear strength of transition-metal dichalcogenides and graphene. *Phys Rev B* **92**(8): 085434 (2015)

[34] Gao W, Tkatchenko A. Sliding mechanisms in multilayered hexagonal boron nitride and graphene: The effects of directionality, thickness, and sliding constraints. *Phys Rev Lett* **114**(9): 096101 (2015)

[35] Zhan H, Tan X F, Xie G X, Guo D. Reduced fracture strength of 2D materials induced by interlayer friction. *Small* **17**(13): 2005996 (2021)

[36] Tan X F, Guo D, Luo J B. Dynamic friction energy dissipation and enhanced contrast in high frequency bimodal atomic force microscopy. *Friction* **10**(5): 748–761 (2022)

[37] Sattari Baboukani B, Ye Z J, Reyes K G, Nalam P C. Prediction of nanoscale friction for two-dimensional materials using a machine learning approach. *Tribol Lett* **68**(2): 57 (2020)

[38] Wang C Q, Chen W G, Zhang Y S, Sun Q, Jia Y. Effects of vdW interaction and electric field on friction in MoS_2. *Tribol Lett* **59**(1): 7 (2015)

Jianbin LUO. He received his B.E. degree from Northeastern University, China, in 1982, and got his M.E. degree from Xi'an University of Architecture and Technology, China, in 1988. In 1994, he received his Ph.D. degree from Tsinghua University, China, and then joined the faculty of Tsinghua University, China. Prof. LUO has been engaged in the research of thin film lubrication and superlubricity. He is currently an academician of Chinese Academy of Sciences, China, and a Yangtze River Scholar Distinguished Professor of Tsinghua University, China. He was awarded the STLE International Award (2013), the CTI highest achievement award (2013), the Chinese National Technology Progress Prize (2008), the Chinese National Natural Science Prize (2001 and 2018), and the Chinese National Invention. He has made keynote or plenary talks for 30 times on the international conferences.

Xinfeng TAN. He obtained his B.E. degree from Beihang University, China, in 2015, and received his Ph.D. degree in mechanical engineering in 2020 from Tsinghua University, China. He is now working as a research assistant at State Key Laboratory of Tribology in Advanced Equipment, Tsinghua University, China. His research interests include the dynamic friction energy dissipation detection at micro-nano scale as well as the design and improvement of micro-nano tribometer based on the AFM.

Lina ZHANG. She obtained her B.S. degree from Northeastern University, China, in 2019. Currently, she is a Ph.D. candidate in State Key Laboratory of Tribology in Advanced Equipment, Tsinghua University, China. Her research focuses on the friction behavior and mechanism study of 2D materials in nanoscale.